

Optical coherence tomography for quality assessment of embedded microchannels in alumina ceramic

Rong Su,^{1,*} Mikhail Kirillin,² Peter Ekberg,¹ Arne Roos,³ Ekaterina Sergeeva,² and Lars Mattsson¹

¹Department of Production Engineering, the Royal Institute of Technology, 68 Brinellvägen, Stockholm 10044, Sweden

²Laboratory of Biophotonics, Institute of Applied Physics RAS, 46 Ulyanov str., Nizhny Novgorod 603950, Russia

³The Angstrom Laboratory, Uppsala University, Box 534, Uppsala 75121, Sweden

*rong.su@iip.kth.se

Abstract: Large-scale and cost-effective manufacturing of ceramic micro devices based on tape stacking requires the development of inspection systems to perform high-resolution in-process quality control of embedded manufactured cavities, metal structures and defects. With an optical coherence tomography (OCT) system operating at 1.3 μm and a dedicated automated line segmentation algorithm, layer thicknesses can be measured and laser-machined channels can be verified in alumina ceramics embedded at around 100 μm depth. Monte Carlo simulations are employed to analyze the abilities of OCT in imaging of the embedded channels. The light scattering parameters required as input data for simulations are evaluated from the integrating sphere measurements of collimated and diffuse transmittance spectra using a reconstruction algorithm based on refined diffusion approximation approach.

©2012 Optical Society of America

OCIS codes: (110.4500) Optical coherence tomography; (120.4290) Nondestructive testing; (110.0113) Imaging through turbid media; (290.0290) Scattering; (100.0100) Image processing; (000.4430) Numerical approximation and analysis.

References and links

1. S. Bredeau and L. Federzoni, "Multilayer: a large scale production of micro devices via new rolled multi material layered 3D shaping technology," in *Proceedings of the 4M/ICOMM 2009 Conference*, V. Saile, K.Ehmann and S. Dimov, ed. (Karlsruhe, 2009), 419–422.
2. A. S. Birks and R. E. Green, *Ultrasonic Testing 2nd ed* (Columbus, 1991).
3. P. Zinin and W. Weise, "Theory and applications of acoustic microscopy", in *Ultrasonic Nondestructive Evaluation: Engineering and Biological Material Characterization*, T. Kundu, ed. (CRC Press, Boca Raton, 2003)
4. N. Chawla, J. J. Williams, X. Deng, C. McClimon, L. Hunter, and S. H. Lau, "Three-dimensional characterization and modeling of porosity in powder metallurgical steels," *Int. J. Powder Metall.* **45**, 19–28 (2009).
5. S. R. Stock, *MicroComputed Tomography: Methodology and Applications* (CRC Press, 2008).
6. B. E. Bouma and G. J. Tearney, *Handbook of Optical Coherence Tomography*, (Marcel Dekker, 2002).
7. A. F. Fercher, W. Drexler, C. K. Hitzenberger, and T. Lasser, "Optical coherence tomography—principles and applications," *Rep. Prog. Phys.* **66**(2), 239–303 (2003).
8. M. Wojtkowski, "High-speed optical coherence tomography: basics and applications," *Appl. Opt.* **49**(16), D30–D61 (2010).
9. C. S. Colley, J. C. Hebden, D. T. Delpy, A. D. Cambrey, R. A. Brown, E. A. Zibik, W. H. Ng, L. R. Wilson, and J. W. Cockburn, "Mid-infrared optical coherence tomography," *Rev. Sci. Instrum.* **78**(12), 123108 (2007).
10. D. Stifter, "Beyond biomedicine: a review of alternative applications and developments for optical coherence tomography," *Appl. Phys. B* **88**(3), 337–357 (2007).
11. M. Yu. Kirillin, E. Alarousu, T. Fabritius, R. Myllylä, and A. V. Priezzhev, "Visualization of paper structure by optical coherence tomography: Monte Carlo simulations and experimental study", *J. Eur. Opt. Soc.- Rapid Publ.* **2**, 07031 (2007).
12. M. Bashkansky, M. D. Duncan, M. Kahn, D. Lewis III, and J. Reintjes, "Subsurface defect detection in ceramics by high-speed high-resolution optical coherent tomography," *Opt. Lett.* **22**(1), 61–63 (1997).

13. M. D. Duncan, M. Bashkansky, and J. Reintjes, "Subsurface defect detection in materials using optical coherence tomography," *Opt. Express* **2**(13), 540–545 (1998).
14. M. Bashkansky, D. Lewis III, V. Pujari, J. Reintjes, and H. Y. Yu, "Subsurface detection and characterization of Hertzian cracks in Si₃N₄ balls using optical coherence tomography," *NDT Int.* **34**(8), 547–555 (2001).
15. J. Veilleux, C. Moreau, D. Lévesque, M. Dufour, and M. I. And, "Boulos," "Optical coherence tomography for inspection of highly scattering ceramic media: glass powders and plasma-sprayed coatings," *Rev. Quantitative Nondestruct. Eval.* **25**, 1059–1066 (2006).
16. J. Manara, R. Caps, F. Raether, and J. Fricke, "Characterization of the pore structure of alumina ceramics by diffuse radiation propagation in the near infrared," *Opt. Commun.* **168**(1–4), 237–250 (1999).
17. J. G. J. Peelen and R. Metselaar, "Light scattering by pores in polycrystalline materials: Transmission properties of alumina," *J. Appl. Phys.* **45**(1), 216–220 (1974).
18. R. Apetz and M. P. B. van Bruggen, "Transparent alumina: a light-scattering model," *J. Am. Ceram. Soc.* **86**(3), 480–486 (2003).
19. W. F. Cheong, S. A. Prahl, and A. J. Welch, "A review of the optical properties of biological tissues," *IEEE J. Quantum Electron.* **26**(12), 2166–2185 (1990).
20. C. F. Bohren and D. R. Huffman, *Absorption and Scattering of Light by Small Particles* (Wiley-VCH, 1998).
21. C. K. Hitzenberger, A. Baumgartner, and A. F. Fercher, "Dispersion induced multiple signal peak splitting in partial coherence interferometry," *Opt. Commun.* **154**(4), 179–185 (1998).
22. J. M. Schmitt, S. H. Xiang, and K. M. Yung, "Speckle in optical coherence tomography," *J. Biomed. Opt.* **4**(1), 95–105 (1999).
23. A. Ozcan, A. Bilenca, A. E. Desjardins, B. E. Bouma, and G. J. Tearney, "Speckle reduction in optical coherence tomography images using digital filtering," *J. Opt. Soc. Am. A* **24**(7), 1901–1910 (2007).
24. L. Wang, S. L. Jacques, and L. Zheng, "MCML--Monte Carlo modeling of light transport in multi-layered tissues," *Comput. Methods Programs Biomed.* **47**(2), 131–146 (1995).
25. R. K. Wang, "Signal degradation by multiple scattering in optical coherence tomography of dense tissue: a Monte Carlo study towards optical clearing of biotissues," *Phys. Med. Biol.* **47**(13), 2281–2299 (2002).
26. M. Kirillin, I. Meglinski, V. Kuzmin, E. Sergeeva, and R. Myllylä, "Simulation of optical coherence tomography images by Monte Carlo modeling based on polarization vector approach," *Opt. Express* **18**(21), 21714–21724 (2010).
27. Swerea IVF, Mölndal (head office), P O Box 104, SE-431 22 Mölndal, Sweden.
28. I. H. Malitson, F. V. Murphy, and W. S. Rodeny, "Refractive index of synthetic sapphire," *J. Opt. Soc. Am.* **48**, 72 (1958).
29. A. Ishimaru, *Wave Propagation and Scattering in Random Media*, vol.1 (Plenum Press, New York, 1978).
30. R. C. Haskell, L. O. Svaasand, T.-T. Tsay, T.-C. Feng, M. S. McAdams, and B. J. Tromberg, "Boundary conditions for the diffusion equation in radiative transfer," *J. Opt. Soc. Am. A* **11**(10), 2727–2741 (1994).
31. L. S. Dolin and E. A. Sergeeva, "A model of irradiance distribution for a directed point source in an infinite weakly absorbing turbid medium," *Radiophys. Quantum Electron.* **44**(11), 858–865 (2001).
32. R. C. Gonzalez and R. E. Woods, *Digital Image Processing 3rd edition* (Prentice Hall, 2008).
33. A. Roos, "Use of an integrating sphere in solar energy research," *Sol. Energy Mater. Sol. Cells* **30**(1), 77–94 (1993).
34. C. Pecharromás, G. Mata-Osoro, L. A. Díaz, R. Torrecillas, and J. S. Moya, "On the transparency of nanostructured alumina: Rayleigh-Gans model for anisotropic spheres," *Opt. Express* **17**(8), 6899–6912 (2009).
35. R. Su and L. Mattsson, Depth profiling in alumina ceramic by optical coherence tomography," in *Proceedings of the 4M 2010 Conference*, B Fillon, C. Khan-Malek, S. Dimov, ed., (Bourg en Bresse, 2010), 316–319.
36. S. K. Kachigan, *Statistical Analysis* (Radius Press, 1986).
37. L. Mattsson, V. Schulze, and J. Schneider, *Ceramics Processing in Microtechnology* (Whittles Publishing, 2009), Chap. 22.
38. Thorlabs Sweden AB, Mölndalsvägen 3, 400 20 Gothenburg, Sweden.

1. Introduction

The emerging markets of non-silicon multimaterial micro devices offer a great potential for commercialization in the near future. However, the manufacturing process for complex multifunctional ceramic 3D parts is still in an early stage and in parallel with the current development of the solution for 'roll-to-roll manufacturing of ceramic micro devices' based on tape casting and advanced printing techniques, there is a need for development of inspection systems [1]. These systems need to perform quality inspection of embedded micro channels and metal connections and they must be able to detect delaminations and other defects as well within a sintered multi-layer ceramic stack rolling out from a hot sintering process.

Alumina, i.e. aluminum oxide, is one of the most common materials used in ceramic manufacturing. In the tape casting business for micromanufacturing it is a good candidate for producing microwave components for terahertz applications, where low loss at high frequencies and low surface roughness are expected. Its relatively high thermal conductivity

is an advantage when making coolers for automotive lighting systems, and alumina has been chosen for micro fluidic devices for micro reactors, fuel cells or medical devices due to the hardness as well as the stability against chemical attack, high temperatures, thermal shock and abrasion [1]. The manufacturing processes to be controlled include tape casting, tape structuring, printing, lamination, and sintering. This paper concentrates on the thickness control of the alumina layer in tape casting and the dimensional quality inspection of embedded laser machined channels with tolerances in the ten micron range. In the terahertz components for example, the variation in thickness can affect the dielectric loss. Regarding the coolers for automotive lighting systems the dimensional quality is designed for getting the best heat dissipation from the surface and LED system. For microfluidic devices, the flow parameters of media are influenced by a change of channel dimensions and surface quality. Moreover, defects such as large residual pores in the alumina layer significantly influence the thermal conductivity and mechanical properties of the layers.

The measurement technology has to meet high demands to provide quality assurance, and at the same time address the issues of costs and productivity. The key to success is believed to be a non-contact, non-destructive in-process metrology technique with automated image processing and analysis. An obvious choice is ultrasonic testing and acoustical microscopy [2,3]. It is normally a non-destructive testing method. However, it needs a liquid couplant between the transducer and the ceramic, and is therefore a contamination risk in a roll-to-roll production process of embedded microchannels. X-ray transmission is another well established technique that might work well for embedded heavy metal structures giving good contrast by X-ray absorption [4] but might be troublesome for small open cavities inside the material. X-ray micro tomography [5] is a very promising technique with possible resolution in the micrometer range, but at present the data acquisition time, typically hours, is by far too long to be realistic for in-process metrology.

Optical Coherence Tomography (OCT) [6,7] is in our view the most promising metrology candidate to achieve the key to success in the roll-to-roll manufacturing. It provides a depth profiling of the internal structures of semitransparent samples, offers the advantage of contactless and non-destructive detection, with high image resolution and acquisition rate. By the development of Fourier-domain OCT the imaging speed has exceeded 300,000 A-scans/s [8]. The operating wavelength of OCT is normally from 680 nm to 1.8 μm . One system exists also for the region of 6-8 μm [9]. Except being well-known for tissue investigations in biomedical science, this technique is gradually becoming used in a number of other applications [10,11]. Bashkansky and his group applied OCT to determine the size and distribution of subsurface defects in PZT and Hertzian cracks in silicon nitride ceramics. Other materials like lead zirconate titanate, single-crystal silicon carbide, and Teflon-coated wires have been investigated by the group [12–14]. Later Veilleux et al. [15] used OCT to evaluate the refractive index of Ytria-stabilized zirconia, YSZ, the non-transformable tetragonal phase. However, the feasibility of OCT as a dimensional micro metrology tool for highly scattering ceramics has rarely been studied. In this paper dedicated solutions are developed for high precision and automated in-process industrial metrology of the ceramic micro devices with the application of OCT.

Because of the rather high refractive index of alumina the presence of pores (the main contributor of light scattering in our alumina sample) makes it a turbid media in the visible and the near infrared wavelength regions. Light scattering causes severe problems to observe structures such as cavities and metal connections embedded in the material. The obvious way is to use longer wavelengths, in order to reduce the signal degradation induced by scattering. Spectra of absorption and scattering coefficients in the visible and near-infrared region can be obtained from spectrophotometry measurements of total and diffuse transmittance and reflectance with further processing using the Radiative Transfer Equation and Beer-Lambert law [16–18], or Kubelka Munk theory [19]. Another approach is to calculate the desired spectra employing Mie theory [16–18,20] under the assumption of spherically shaped pores in the material.

When investigating the internal structures in a highly-scattering medium, various noise, light dispersion and speckle degrade the quality of OCT images [21,22]. The boundaries between materials become blurred, which increases measurement uncertainty and difficulty of feature recognition in the micro-scale metrology. Some physical approaches and digital algorithms have been applied to enhance the image quality and contrast [22,23]. However, by using the polarization diversity method the actual increase in signal to noise ratio, SNR, that can be realized in OCT may be quite small [22]. As a trade-off spatial compounding technique results in some loss of resolution [22]. And the use of a large NA of the microscope lens could limit the capability of OCT for detecting high aspect-ratio features in micro ceramics devices. For frequency compounding, a simple technique without loss of axial resolution has not been developed [22]. In particular, OCT systems operating at longer wavelengths have the possibility to provide larger probing depth in ceramic materials, but the difficulty is the radiation source spectrum that needs to be even wider to keep the axial resolution.

Indeed the speckle reduction methods can increase the SNR in OCT image to some extent, but so far some loss of useful information is inevitable. The degradation of measurement accuracy is not traceable without knowledge of the losses. Therefore, we introduce in this paper a simple and automated line segmentation method which is dedicated to recognize surfaces, embedded boundaries and features in OCT images, and simultaneously remains the useful information. The application of this algorithm can replace human's observation and improve measurement precision of OCT detection, in order to meet the future demand of the in-process 3D monitoring of ceramic micro devices.

Furthermore, in order to fully exploit the potential of OCT for alumina ceramic materials and to understand the formation of the image, a thorough simulation study has been conducted based on the Monte Carlo method [24], which has been widely used in the simulations of OCT images [25,26]. The input parameters for Monte Carlo simulations are taken from the reconstructed spectra of optical properties. In this paper a dedicated model with structures based on a real sample is built up along with inputting the geometrical shapes, dimensional parameters, refractive index, and light scattering parameters. The simulation results are considered as a reference of the adequacy of predicting future inspection possibilities for different embedded geometries and depths and also provide a convincing proof for the feasibility of OCT in the industrial metrology of ceramic micro devices.

2. Materials and methods

2.1 Alumina ceramic samples

The alumina samples MLA100 and SAL1 used in our study were provided by Swerea IVF [27]. 0.3 weight percentage (with respect to alumina weight) dispersant (Dispex A40) was used, and the green tape contained 22% latex binder (LDM 7665S, Celanese). After sintering at 1630°C for 30 hours the binder was burnt away.

The channel in SAL1 was cut with Nd-YAG laser (wavelength 1064 nm, beam diameter around 90 μm) at Thickfilm Microsystems Laboratory, Wrocław University of Technology. The variation of the laser beam diameter is around $\pm 10 \mu\text{m}$, and the channel width and depth were approximately 160 μm and 100 μm , respectively.

2.1.1 Microstructure of alumina ceramics

The SEM images provided by Swerea IVF were used to study the micro structures of sintered alumina samples. Figure 1 shows the prepared cross-section of sample MLA100. The residual pores that are assumed to be filled with air are distributed randomly in the alumina matrix. Pores appearing inside the grains tend to have circular cross-sections, indicating spherical pores, while the pores appearing at the boundaries between grains can be randomly shaped and are relatively larger.

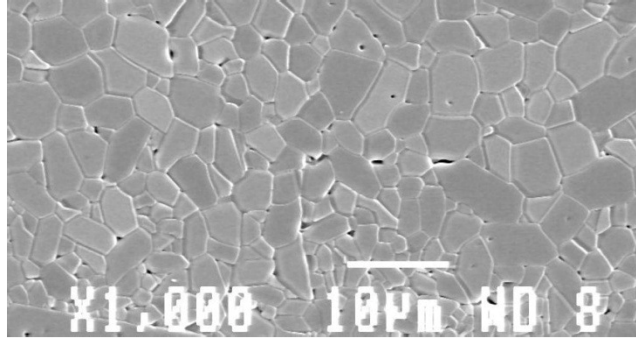


Fig. 1. SEM image of the prepared cross-section of sample MLA100.

The volume porosity is calculated by $1 - (d_s/d_{theo})$, where d_s is the density of the sample (3.909g/cm^3), and d_{theo} is the theoretical density of alumina (3.98g/cm^3). The average pore diameter is still difficult to obtain, but it can be estimated using the area porosity obtained from the SEM image if spherical pores are assumed [18]. The porosity and average pore diameter of the sample MLA100 are then obtained as $\sim 1.8\%$ and $0.56\ \mu\text{m}$.

2.1.2. Refractive index of alumina

As shown in Fig. 2 the values of both the real and imaginary parts of the refractive index of alumina were picked from data published in [28] for the wavelength range $1\text{-}7\ \mu\text{m}$. The data of the real part of the refractive index, n , agree well with the calculation results from [17]

$$n = \left(1 + \frac{1.023798 \times \lambda^2}{\lambda^2 - 0.00377588} + \frac{1.058264 \times \lambda^2}{\lambda^2 + 0.0122544} + \frac{5.280792 \times \lambda^2}{\lambda^2 - 321.3616}\right)^{1/2} \quad (1)$$

where λ is the wavelength of the incident light expressed in micrometers. The imaginary part of the refractive index, the extinction coefficient k , representing absorption, is very close to zero in the $0.3\text{-}4\ \mu\text{m}$ range.

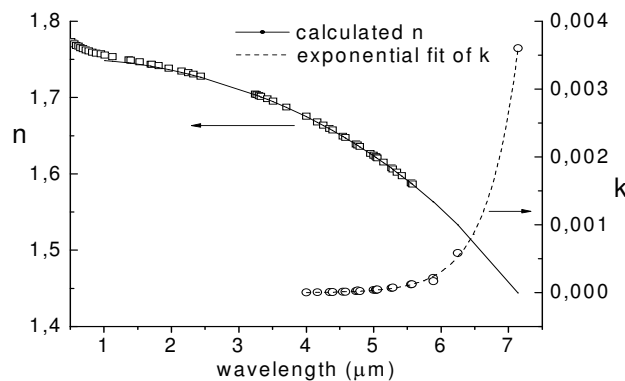


Fig. 2. Real (n) and imaginary (k) part of the refractive index of alumina

2.2. Methods of optical characterization and measurement

2.2.1. Spectrophotometry measurement

For our alumina samples, the discontinuity in the refractive index between the alumina ceramic matrix of grains of about $3\ \mu\text{m}$ size and the embedded air-filled pores are considered as the main cause for the turbid behavior of our alumina samples. Therefore the analysis of transmittance and reflectance spectra obtained from spectrophotometry

measurements offer an opportunity for the calculation of light scattering parameters and, hence, to find a suitable wavelength window where the alumina is more transparent. A Perkin Elmer Lambda900 spectrophotometer with double beam and double monochromator was used for the wavelength range 0.3 - 2.5 μm . The spectrophotometer was equipped with a 150 mm spectralon integrating sphere, allowing total and diffuse spectra to be recorded both for reflectance and transmittance. The recorded spectra were corrected for the sphere wall reflectance when necessary.

2.2.2. OCT imaging

OCT basically synthesizes 2D images from a series of adjacent low coherence interferometry in-depth-scans. The detailed principles of OCT can be found in [6,7]. For time demanding in-process inspection, the Fourier-domain OCT (including spectral OCT and swept-source OCT) is preferred because no mechanical motion for in-depth-scanning is required [8]. Instead the in-depth information is obtained by Fourier transformation of the spectral response. In this study a Thorlabs 1325nm swept-source OCT was used to image the alumina samples. The specification of this OCT system is listed in Table 1.

Table 1. Specification of Thorlabs 1325nm swept-source OCT [38]

Center Wavelength	Spectral Bandwidth	Axial Scan Rate	Imaging Width	Imaging Depth	Transverse Resolution	Axial Resolution
1325 nm	>100nm	16 kHz	6.0 mm (1024 pixels)	3.0 mm (512 pixels)	25 μm	12 μm (in air)

2.3. Light scattering model

2.3.1. Theory

Due to the extremely low extinction coefficient of alumina in the visible and near-infrared region the absorption is negligible. Scattering makes the embedded features fuzzy, and the reduced image contrast introduces uncertainties in the measurements of dimensions of microstructures and failures in inspecting the defects. In order to simulate these effects in an OCT system we need to evaluate the scattering properties of our particular samples.

With the knowledge of the porosity of sintered alumina ceramics, its average pore size and under the assumption of nearly spherical pores, the Mie scattering model [17,20] can be used to estimate scattering coefficient μ_s and scattering anisotropy factor g which represents the mean cosine of the scattering angle [29]. However, accurate estimation of scattering parameters by the Mie model requires information on pore distribution, pore size and shape. This can potentially be obtained from a thorough analysis of the ceramics microstructure. An alternative way to assess the required scattering parameters (μ_s and g) is the measurement of collimated transmittance, often referred to as in-line transmittance in optical assessment of ceramics, and diffuse transmittance/reflectance, followed by numerical reconstruction of the desired parameters. Measurement of the collimated transmittance in VIS-NIR allows us to evaluate the total scattering coefficient μ_s using Beer-Lambert law. Calculation of the scattering anisotropy factor g can be performed from the reduced scattering coefficient $\mu_s' = \mu_s(1-g)$ which is the only parameter governing the light diffusion in the case of negligible absorption. Usually, reconstruction of μ_s' is based on Kubelka-Munk two-flux theory [19] from the measured diffuse reflectance or transmittance. Unfortunately, this approach does not account for refractive index mismatch at the boundaries of the examined sample, which is quite significant for highly refractive alumina ceramics. Such a mismatch can be effectively accounted for when light propagation in highly turbid medium is considered in the framework of the diffusion approximation of radiation transport theory [29,30]. However, the latter is valid only for optically thick samples when the power of collimated transmittance is typically below noise level which leads to unreliable values of reconstructed μ_s . Therefore we developed a new theoretical model which allows us to embed non-scattered and least scattered light into the diffusion approximation. This makes the model valid for both low-

scattering as well as highly scattering samples [31]. The model also takes the sample/air refractive index mismatch into account. Using this model, the coefficients of diffuse transmittance (T_d) and reflectance (R_d) in a non-absorbing sample of thickness l can be calculated as follows:

$$T_d = T_F \left[T_F \exp(-\mu_s' l) + \frac{2m+3}{3\mu_s' l + 4m} + \left(\frac{2m-3}{3\mu_s' l + 4m} - 1 \right) \exp(-\mu_s' l) \right], \quad (2)$$

$$R_d = R_F \left[1 + T_F^2 \exp(-2\mu_s' l) \right] + T_F^2 \left[1 - \frac{2m+3 + (2m-3) \exp(-\mu_s' l)}{3\mu_s' l + 4m} \right]. \quad (3)$$

Here T_F and R_F are the Fresnel transmission and reflection coefficients respectively, for normal incidence of the light from air onto the sample with refractive index n . The parameter m is described by the formula [30,31]:

$$m = \frac{1 + 3 \int_0^{\pi/2} R_F(\theta, n) \cos^2 \theta \sin \theta d\theta}{1 - 2 \int_0^{\pi/2} R_F(\theta, n) \cos \theta \sin \theta d\theta}. \quad (4)$$

Where $R_F(\theta)$ is the dependence of Fresnel reflection coefficient on the incidence angle. Note that in the case of non-absorbing medium $T_d + R_d = 1$. The collimated transmittance T_c can be expressed using Beer-Labmert law with account for refractive index mismatch at the sample boundary in the following way:

$$T_c = T_F^2 \exp(-\mu_s l). \quad (5)$$

As a result the Eqs. (2),(5) or (3),(5) allow us to evaluate the parameters μ_s and μ_s' (and hence, μ_s and $g = 1 - \mu_s'/\mu_s$) from the integrating sphere measurements.

2.3.2. Monte Carlo simulations

With the significant improvement of computing capability, the numerical simulation of the photon transportation in turbid media can be performed by applying the Monte Carlo (MC) method [24], which in application to light propagation in turbid media consists in numerous simulation of photons random trajectories based on the optical properties and geometry of the object and further statistical analysis of the obtained results. For simulation of the OCT images of alumina ceramics presented here we used the Monte Carlo code developed and tested in previous studies [11,26].

2.4. Post processing of OCT image

Experimentally captured OCT images are in many applications quite noisy due to speckles and they are often analysed visually and qualitatively. In our case we are aiming for developing OCT as an accurate and quantitative metrology tool. Therefore we put much effort into developing a dedicated line segmentation method that includes filtering, scattering peak detection and segmentation, in order to process the massive data from OCT detection in a fast and robust way. It is used to extract lines corresponding to the interfaces in the layered alumina stacks and other feature boundaries embedded in the ceramic. Due to the expected acquisition speed we have to accept processing of noisy single scan OCT images. A proper thresholding of the filtered image combined with an advanced statistical treatment of local neighbourhood of pixels is our successful approach to find and localize the backscattering peaks with sub-pixel precision.

In the first step a so-called filtering kernel is used to reduce noise in the image. Depending on the noise characteristics many different noise reduction methods can be used

[32]. We have found that an ordinary Gaussian filter can be used without losing information of location of the interface borders. In addition an image pyramid filter [32] is used to level the linear decay of the intensity profile expressed in dB of the OCT images.

For backscattering peak detection from the interfaces and feature boundaries a so-called pixel map [32] is generated. This 2D map contains all pixels that are probable candidates for contributing to the continuous backscattering peak in the original image. The algorithm uses as much information as possible in all neighbouring pixels close to the peak to estimate the “best average” location of the peak. In this process the 2D map is the input to a sub-pixel precision estimation algorithm in the original non-filtered OCT image. By using a large number of pixels around a candidate pixel the variance of the estimated location of the local average peak is minimized. As shown in Fig. 3, the sub-pixel precision algorithm estimates the gradients of eight neighbouring pixels. These gradient vectors are presented as black arrows, and the opinions of the locations of the intensity maxima are marked with small gray dots. These gradients are then used for a better estimation of the boundary location in sub-pixel precision (marked with hair cross).

After the peak detection step all local maxima are clustered together in bins. The centre position of each bin is given by the Centre of Gravity (COG) of the local maxima in the bin [32]. The size of the bin is the same as the pixel resolution of the original image, i.e. 1×1 pixels. This clustering reduces the data of the local peak maxima dramatically without any loss of information.

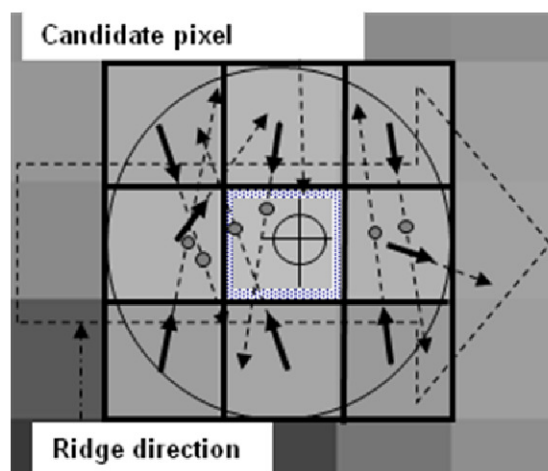


Fig. 3. Schematic of the sub-pixel precision estimation algorithm. The hair cross is the estimated sub-pixel location of the candidate pixel in the middle. An individual neighbour’s opinion must be inside the large circle to be accepted.

In the segmentation step the pixels describing a boundary were connected into a line segment, i.e. a continuous set of local peak maxima [32]. We divided the direction of the boundaries into angular intervals and built line segments of the boundaries within a certain angle. High-precision measurements can then be made between the line segments having the same direction, e.g. for measuring the layer thickness or interface distances within the ceramic.

3. Results and discussions

3.1. Spectrophotometry measurement

The spectra of total and diffuse transmittance and total reflectance of the sintered alumina sample MLA100 are shown in Fig. 4. For most wavelengths the stability of the signal is within 0.1% (for both transmittance and reflectance), but close to the detector change at $\lambda = 860$ nm the signal gets more noisy. The sum of the total transmittance and reflectance is

approximately 100%, which means there is no absorption in the wavelength region from 500 – 2000 nm. The total transmittance increases almost linearly with the wavelength, while the diffuse transmittance peaks at around 1000 nm and then decreases gradually, indicating that less scattering events occur. Spectrum of collimated transmittance can be calculated as the difference between the spectra of total and diffuse transmittance. The measured signals are corrected for the reference surface reflectance and the integrating sphere wall. Details of the methods can be found in [33].

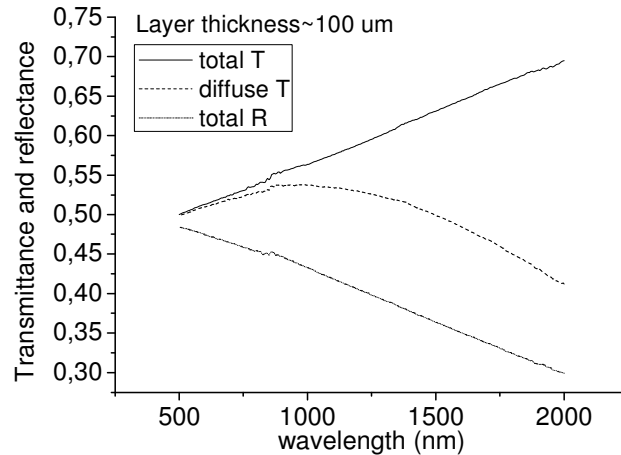


Fig. 4. Total and diffuse transmittance and total reflectance of the sintered alumina sample

From the spectrophotometer data the scattering coefficient and anisotropy factor g were calculated by the theoretical model described in section 2.3.1 [31], as well as by Mie scattering model. For the Mie-calculations the porosity of 1.8% and average pore diameter of $0.56 \mu\text{m}$ were used. In Fig. 5 the scattering coefficient obtained by both two models decreases gradually with the wavelength, and it can be expected to be even lower at longer wavelength due to the decrease of the refractive index of alumina. However, most of the existing OCT systems operate below $2 \mu\text{m}$ except one system working at $6\text{-}8 \mu\text{m}$. From Fig. 2 the extinction coefficient of alumina starts to rise from $5 \mu\text{m}$, and therefore absorption may limit the performance of this OCT.

It is notable that the Mie model, assuming spherical pores with a fixed size yields considerably higher scattering coefficients, in particular at wavelengths $< 1.5 \mu\text{m}$, and a peak at $0.56 \mu\text{m}$ due to resonant oscillation when the wavelength close to the pore size. Moreover, the scattering coefficient calculated by Mie model decreases faster with wavelength than that obtained by the light diffusion model.

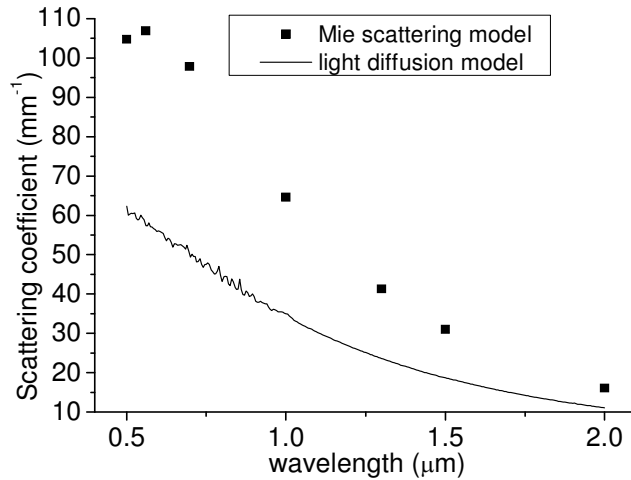


Fig. 5. Scattering coefficients of sintered alumina calculated by the Mie scattering model using porosity and pore size estimations (filled dots), and by the light diffusion model using measured spectra of collimated and diffuse transmittance (line).

The g -factor representing the mean cosine of the scattering angle is plotted in Fig. 6 for both calculations. The Mie model yields higher g -values at shorter wavelengths, but with the increase of wavelength the g -value decreases much faster than that obtained by the light diffusion model. These facts show the Mie model assuming spherical pores with a fixed size is not realistic and cannot give accurate scattering parameters [17]. Moreover, Mie model does not take into account the preferential orientation of grain's c -axis that may also contribute to the scattering [34]. However, it is not proper either to only consider light scattering from grain boundaries using the Rayleigh-Gans-Debye approximation, particularly in our case where the alumina samples contain larger grains and much more pores compared to the case in [34]. Thus, the scattering parameters obtained by the light diffusion model are considered more accurate to be used in Monte Carlo simulation of OCT images.

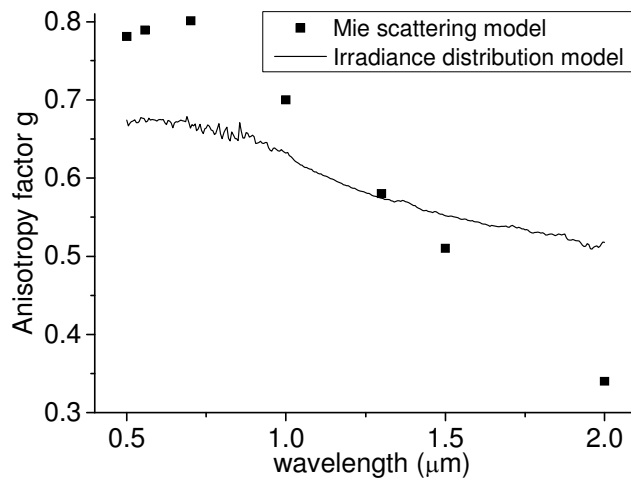


Fig. 6. Anisotropy factor g of sintered alumina calculated by the Mie scattering model using porosity and pore size estimations (filled dots), and by the light diffusion model using measured spectra of collimated and diffuse transmittance (line).

3.2. OCT imaging of alumina sample structure

The depth profile of the stacked alumina layers is clearly resolved by the OCT measurement, as seen in Fig. 7. An embedded channel is simulated by covering the channel layer with another alumina layer but the two layers are not bonded. Thus an air gap can be found which simulates delamination between the two layers. The top layer is the sintered MLA100 alumina with a thickness of $101 \pm 4.5 \mu\text{m}$ over the entire $3 \times 6 \text{ cm}^2$ (accurately measured with an inductive spherical probe towards a spherical ball to minimize waviness contribution to the thickness measurement). The second layer is the SAL1 alumina with a laser-machined channel in the upper surface. The direction of the channel is perpendicular to the figure plane, i.e. the cross section is seen in the image. Both the upper and lower boundaries of the top layer MLA100 can be observed with a good imaging contrast. The upper surface of SAL1 with the laser machined channel is found below an air gap formed by the non-flat surfaces. For these samples the effective scattering coefficient at $\lambda = 1.3 \mu\text{m}$ limits the probing depth to an optical thickness of about $450 \mu\text{m}$ [35].

The black area at the top in the image with randomly distributed noise corresponds to the air, where the noise comes from speckles [6,8]. This noise contributes to the total signal in the Fourier-domain OCT, and also affects the imaging contrast of the measured samples. Because of the discontinuity of the refractive index between the air and alumina, the backscattering from the top surface of MLA100 contributes to the first intensity peak of the OCT signal. However the high intensity of the specular reflection can give rise to a fuzzy area above the first surface. It can be partially avoided by adding an optical clearing medium to the object surface or by tilting the samples [6,8].

In Fig. 7 the horizontal interfaces appear quite broad. The reason for this is fourfold. 1) The OCT system acquires the logarithm of the intensity, and the unit of the signal is represented in dB in order to increase the imaging contrast, but for the area containing very high intensity the visual contrast for the eye is reduced. 2) A regular commercial OCT system has a depth resolution around $12 \mu\text{m}$ which is limited by the coherence length of the light source, and the vertical pixel resolution is around $6 \mu\text{m}$. A boundary should at least have 1 pixel in depth. 3) Dispersion in the sample under investigation is known to increase the width of the coherence envelope and therefore to decrease the depth resolution in the OCT. It may even induce double peaks from a single interface [21]. 4) Near-ballistic photons that are backscattered from an embedded boundary and have experienced a few small-angle or straight forward scatterings but still fulfil the detection conditions. These photons actually correspond to a larger embedded depth and are accounted for as the ones carrying the depth information of the boundary.

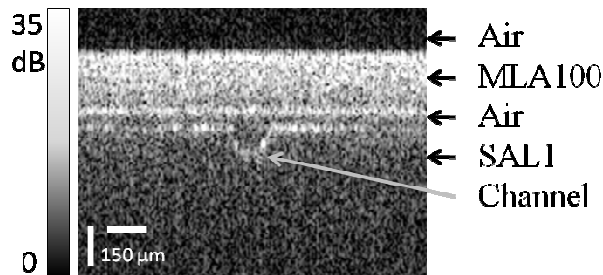


Fig. 7. Cross-sectional OCT image of the stacked and sintered alumina layers MLA100, $\sim 100 \mu\text{m}$ geometrical thickness, and SAL1 with its laser machined channel. Note that the air filled space and channel is imaged with its geometrical size while the upper layer MLA100 is expanded in height by the average refractive index of the alumina at $\lambda = 1.3 \mu\text{m}$. The vertical $150 \mu\text{m}$ scale mark is therefore valid in the air gap only.

3.3. Image processing for metrology applications

As discussed above noise degrades the image contrast of the boundaries that need to be resolved and measured. In addition broadening effect makes it difficult to directly and precisely measure the dimensions between boundaries from an original OCT image. Although the averaged OCT A-scans can present the boundary location as the signal peak, the axial resolution can be reduced and the access to lateral dimensions is not possible without transverse scanning.

Using the line segmentation method described in section 2.4, the original OCT image (Fig. 7) is filtered and the 2D pixel map is generated (Fig. 8), where all bright pixels are candidates for the estimation of continuous boundary peaks. In the last step of the segmentation, shown in Fig. 9, the front and rear boundaries of the top layer and the upper surface of the second layer are represented as two lines. In this magnified picture it is easily seen that the bin locations (marked as crosses) and the extracted lines overlapping on the boundaries in OCT image. The precision of the segmentation method is evident from the comparison with averaged A-scans and the small variation in height position of the bin locations, despite the very poor signal to noise ratio.

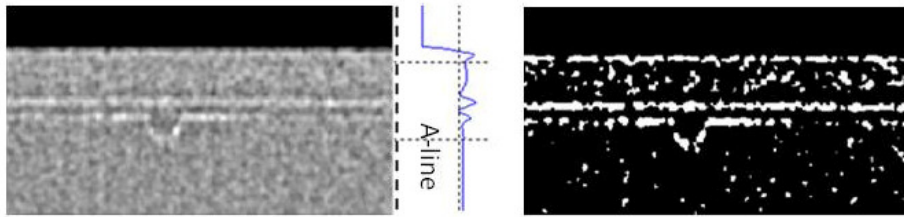


Fig. 8. Filtered OCT cross-sectional image with its intensity profile (left) and the pixel map generated from the filtered image (right).

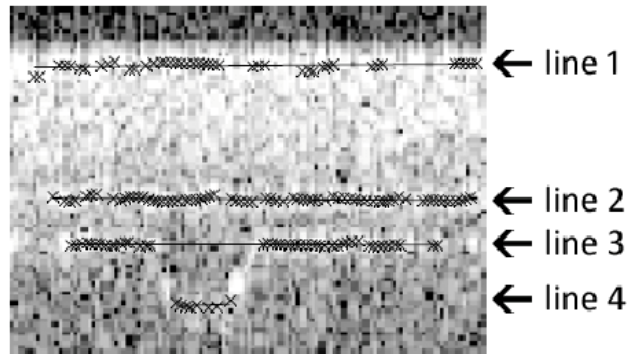


Fig. 9. Post processing of measured OCT image. The three maximum scattering peaks represented as line segments.

From Fig. 9 the measured thickness of the top layer is $101.9 \mu\text{m}$ from the distance between line1 and line2. The refractive index ($n = n_{\text{alumina}} \times (1 - \text{porosity}) + n_{\text{air}} \times \text{porosity}$) is 1.73 and the pixel resolution is $5.86 \mu\text{m}/\text{pixel}$ in vertical depth direction. The uncertainty is analyzed and the results are presented in Table 2, where the depth locations of lines are expressed in pixel positions, and the (0,0) pixel is in the upper left corner of Fig. 9. The uncertainty of the line location is calculated based on the central limit theorem [36] as $\sigma_{\text{line}} = \sigma_{\text{var}} \times m^{-1/2}$ where m is the number of pixels constituting the line, and σ_{var} is the variance of the local COGs relative to the location of the line. With 99.7% confidence, we can determine the thickness of the top layer with 3σ uncertainty ($\sigma^2 = \sigma_{\text{line1}}^2 + \sigma_{\text{line2}}^2$) as $101.9 \pm 2.1 \mu\text{m}$ (the uncertainty of thickness measurement is increased by a factor of $\sqrt{2}$ because the layer

contains two uncorrelated lines). Similarly, the dimension of the air gap obtained from the algorithm is $58.6 \pm 2.0 \mu\text{m}$, and the depth of the channel is $78.6 \pm 2.1 \mu\text{m}$.

Table 2. Dimensional measurements at different depths and uncertainty analysis

Line	Number of pixels constituting a line	Line location in depth (pixel)	σ_{var} (pixel)	σ_{line} (pixel)
1	45	13.07	0.64	0.10
2	75	43.17	0.49	0.06
3	48	53.17	0.37	0.05
4	8	66.59	0.30	0.11

The results agree with the values measured from the averaged A-scans, which are $105.5 \pm 8.3 \mu\text{m}$, $58.6 \pm 8.3 \mu\text{m}$, and $82.0 \pm 8.3 \mu\text{m}$ respectively for the thickness of the top layer and the air gap, and the depth of the channel. So far, we have verified that the dedicated algorithm can retrieve the boundary location (in axial direction) from noisy OCT image with sub-pixel precision, and consequently improve the accuracy of the measurement system.

Moreover, as seen in Fig. 9, line3 and line4 and the corresponding extracted pixels overlap on the signal peaks in the OCT image very well. So the width of the channel opening is $169.5 \mu\text{m}$ measured as the lateral distance between the two pixels at the left and right end of the opening part, the width of the channel bottom is $70.7 \mu\text{m}$. Due to the variation in laser beam diameter ($\pm 10 \mu\text{m}$) and pulse energy, the width and depth of the channel vary within some microns at different positions. Therefore in this study there is no direct comparison between the dimensions measured by OCT and by other metrology tools. However, the measurement uncertainty of OCT in lateral direction will be discussed with simulated OCT image where the geometrical dimensions of the embedded channel are known.

The uncertainty analysis in Table 2 proves only the precision of the line segmentation method applied to the measured OCT image. Determination of the absolute uncertainty of the subsurface dimensional metrology using the OCT technique is very complicated and many different sources of measurement errors need to be considered, e.g. errors in the mechanical and optical part of the instrument, the values of refractive indices, as well as image and data processing methods. This task is out of the scope of this paper but it is of utmost importance for the future metrology of embedded structures and requires calibrated specimens to be investigated. In this study we have developed the line segmentation method to minimize the measurement uncertainty of reading OCT images in an easy and fast fashion.

3.4. Simulated OCT images

For the simulation we used the previously developed Monte Carlo code allowing simulation of OCT images [26]. The simulation model of the alumina stack structure is set according to the samples stack in the object inspected in experimental part of the study. The top layer has a thickness of $100\mu\text{m}$, and below a $60\mu\text{m}$ air gap there is a bottom layer with a thickness of $300\mu\text{m}$ and a ladder-shaped channel in the upward facing surface. The channel which has a depth of $90\mu\text{m}$ is $150\mu\text{m}$ wide at the top and $80\mu\text{m}$ wide at the bottom. Moreover, surface roughness is also considered in the simulation in order to achieve better similarity with real OCT measurements. The typical surface roughness Pq (often referred to as rms roughness) of the MLA alumina sample is in the order of 60 nm and 100 nm (over $250 \mu\text{m}$ long traces). The sample geometry and optical properties listed in Table 3 are used as input to the MC simulation. Although the exact parameters of the scanning system of OCT setup are unavailable, we fitted these parameters to provide qualitative fitting with experimental results.

Table 3. Optical properties of alumina and OCT setup parameters used in MC simulation

Optical properties of alumina			Parameters of OCT setup		
Scattering coefficient	Anisotropy factor g	Refractive index	Center wavelength	Transverse resolution	Axial resolution
23.5 mm^{-1}	0.57	1.73	$1.3 \mu\text{m}$	$20 \mu\text{m}$	$12 \mu\text{m}$

*The scattering parameters are obtained from the spectrophotometric data evaluation.

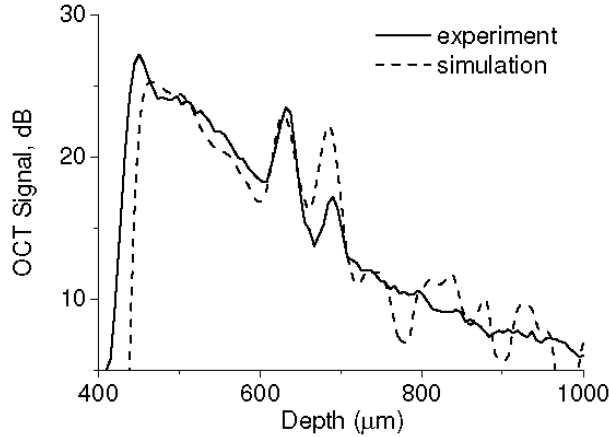


Fig. 10. Comparison between experimental and simulated A-scans (experimental A-scan is averaged over 200 realizations, for simulated A-scan surface rms roughness of 90 nm is used).

In order to make quantitative comparison between experimental and simulated images corresponding A-scans are presented in Fig. 10. From this figure one can see that simulations provide high qualitative agreement with experiment, also some details are different due to unknown details of the optical system of the commercial OCT setup and possible disagreement in considered roughness of the sample surfaces.

The simulated cross-sectional OCT images (Fig. 11a-d) of the alumina stack show the similar intensity distributions as the experimental OCT image, where the intensity of light backscattered from the alumina layers gradually decays with increasing depth. The simulations are performed for a number of roughness values varying from 30 to 140 nm rms roughness. The large mismatch of refractive indices at the alumina-air interface gives rise to the pronounced intensity peak which rises with decrease of alumina surface roughness. The sidewalls of the embedded channel appear to be blurred due to the large angle reflection of incident photons of which only a small fraction suits the detection conditions. Comparing with the experimental OCT image, the simulated results of Fig. 11 (b) and 11(c) with the typical roughness values (90nm and 60nm) provide the best qualitative agreement, while the channel can be hardly detected in Fig. 11 (a) and is too pronounced in (d).

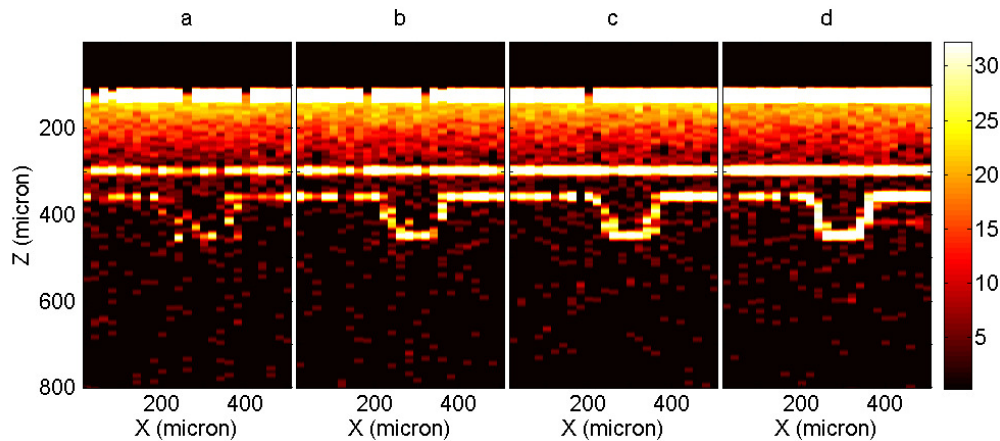


Fig. 11. Simulated cross-sectional OCT images of the stacked alumina layers with embedded microchannel for different rms roughness of the surface: (a) 140 nm, (b) 90 nm, (c) 60 nm, (d) 30 nm.

So far the simulations highly agree with the experiment, which is very much owing to the correctness of the inputted light scattering parameters and material properties. Further, we can start to analyze the simulated images with the dedicated image processing algorithm (as shown in Fig. 12). And the results obtained from the algorithm and the averaged A-scan are listed in Table 4.

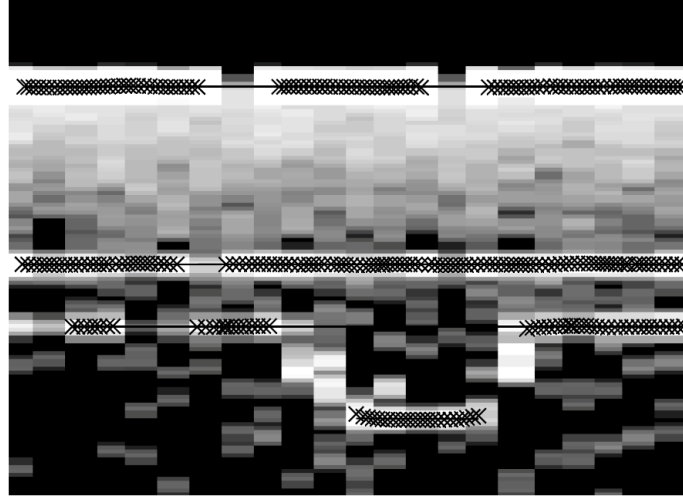


Fig. 12. Post processing of simulated OCT image (rms roughness of 90 nm is used).

Table 4. Optical properties of alumina and OCT setup parameters used in MC simulation

	Top layer thickness	Air gap thickness	Channel depth	Channel width at opening	Channel width at bottom
Image processing algorithm (μm)	100.3 ± 2.0	60.0 ± 2.0	88.7 ± 2.0	160	79
Averaged A-scans (μm)	100 ± 7	60 ± 7	90 ± 7	–	–

*Each pixel corresponds to 5 μm in depth and 20 μm in lateral direction.

The precision of the algorithm is proved again for the in-depth measurements. Furthermore, from the optical perspective we conclude that the OCT imaging through turbid medium provide accurate in-depth measurements in the complex embedded ceramic 3D structure. This means that for in-depth measurements the errors are mainly caused by the mechanical and other optical limitations of the instrument, and/or by operator and environmental factors.

The top-width of the channel measured by the algorithm yields 160 μm and the width of the channel bottom is 79 μm . The measurement uncertainty cannot be evaluated as the width is only determined by the position of two extracted pixels. The top-width is larger than the nominal values. By careful observation of the four corners of the channel in Fig. 12, the edges are blurred by a few pixels in lateral direction at the channel opening and the bottom. This phenomenon can be primarily referred to a very common problem that happens in vision systems. When high accuracy is required, the optical image of an abrupt step (the channel with sharp edge in our case) is not longer a distinct change from black-to-white but rather a continuous intensity change. Careful definition is needed for the grey-level corresponding to the position of the real edge [37]. It will be more difficult to solve this problem in OCT images which are usually very noisy and contain speckles. When imaging through a turbid medium, small-angle multiple-scattered photons scattered back from the sharp edge can also contribute to this phenomenon. Therefore, we conclude that the measurement using OCT without careful calibration can give much larger uncertainty in the lateral direction than in

axial in-depth direction. Reducing the waist radius of the focused (Gaussian) probe beam and increasing the pixel resolution may solve this problem. In this case, the corner position can be found approximately in ± 1 pixel. Thus the widths of the channel opening and bottom (obtained from the positions of two uncorrelated pixels) can be presented as $160 \pm 28 \mu\text{m}$ and $79 \pm 28 \mu\text{m}$, respectively.

4. Conclusion

Progress in ceramic micro manufacturing by stacking ceramic tapes in a roll-to-roll process calls for the development of a non-contact, non-destructive, and in-process automated high quality inspection technique for embedded structures. In this paper we demonstrated the feasibility of using optical coherence tomography at $1.3 \mu\text{m}$ for measuring an embedded microchannel covered by $100\mu\text{m}$ -thick sintered alumina. To enhance the evaluation and allow for accurate geometrical measurements despite poor signal to noise ratios in the OCT images, a dedicated high-precision line segmentation algorithm was developed. This procedure was successfully tested on both experimental OCT images as well as on purposely made Monte Carlo simulated OCT images of the same embedded structure. The input scattering parameters to this simulation was obtained from integrating sphere measurements of collimated and diffuse transmittance of the alumina samples using a reconstruction algorithm based on refined diffusion approximation. The simulation shows that OCT combined with high-precision line segmentation has the potential of measuring thickness and dimensions of the embedded features in an easy and fast fashion, and at the same time provides high accuracy. Further, by simulating other geometrical and optical conditions using the Monte-Carlo OCT technique, we can predict the possibilities of detecting certain features with given tolerance requirements.

Acknowledgments

The authors would like to acknowledge Dr. Johanna Stiernstedt from Swerea IVF, Dominik Jurków from Wrocław University of Technology, and Olle Rosenqvist from Thorlabs Sweden AB. This work is supported by the Multilayer project (FP7-NMP4-2007-214122). M. Kirillin and E. Sergeeva acknowledge the Russian Foundation for Basic Research (Nos. 10-02-00744 and 11-02-01129), grant of the President of the Russian Federation MK-1127.2010.2, and FTP “Scientific and Scientific-Educational Brainpower of Innovative Russia” (projects Nos. 14.740.11.0253, 02.740.11.0839).